Editors' Suggestion

Cryogenic spin Peltier effect detected by a RuO_2-AlO_x on-chip microthermometer

Takashi Kikkawa,[1,*] Haruka Kiguchi,[2,1] Alexey A. Kaverzin,[1,3] Ryo Takahashi,[2] and Eiji Saitoh[1,3,4]

[1] *Department of Applied Physics, The University of Tokyo, Tokyo 113-8656, Japan*
[2] *Department of Physics, Ochanomizu University, Tokyo 112-8610, Japan*
[3] *Institute for AI and Beyond, The University of Tokyo, Tokyo 113-8656, Japan*
[4] *WPI Advanced Institute for Materials Research, Tohoku University, Sendai 980-8577, Japan*

(Received 1 July 2023; revised 4 October 2023; accepted 11 October 2023; published 2 November 2023)

We report electric detection of the spin Peltier effect (SPE) in a bilayer consisting of a Pt film and a $Y_3Fe_5O_{12}$ (YIG) single crystal at the cryogenic temperature T as low as 2 K based on a RuO_2-AlO_x on-chip thermometer film. By means of a reactive co-sputtering technique, we successfully fabricated RuO_2-AlO_x films having a large temperature coefficient of resistance of approximately 100% K^{-1} at around 2 K. By using the RuO_2-AlO_x film as an on-chip temperature sensor for a Pt/YIG device, we observe a SPE-induced temperature change on the order of sub-μK, the sign of which is reversed with respect to the external magnetic field B direction. We found that the SPE signal gradually decreases and converges to zero by increasing B up to 10 T. The result is attributed to the suppression of magnon excitations due to the Zeeman-gap opening in the magnon dispersion of YIG, whose energy much exceeds the thermal energy at 2 K.

DOI: 10.1103/PhysRevApplied.20.054006

I. INTRODUCTION

One of the useful features in spintronics is that various phenomena have been found at room temperature in simple stacked structures, leading to their practical device applications [1–4]. Meanwhile, exploring the spintronic phenomena at low temperatures often resulted in a discovery of additional functional properties with both fundamental and practical prospects [5–11]. A typical example is the spin Seebeck effect (SSE), which refers to the generation of a spin current as a result of a temperature gradient in a magnetic material, and has been observed at room temperature in a variety of magnetic materials, including garnet and spinel ferrites with high magnetic ordering temperatures [12–14]. When SSEs are measured at low temperatures in certain systems however, intriguing physics comes to the surface. Major findings include the signal anomalies induced by hybridized magnon-phonon excitations [14–19], unconventional sign reversal due to competing magnon modes having opposite spin polarizations [20], observation of a spin-superfluid-mediated nonlocal SSE signal [21], and SSEs driven by paramagnetic spins [22,23] and exotic elementary excitations in quantum spin systems [24–26]. Furthermore, recently, a nuclear SSE has been observed in an antiferromagnet having strong hyperfine coupling [14,27]. The signal increases down to ultralow temperatures on the order of 100 mK, which is distinct from conventional thermoelectric effects in electronic (spin) systems [14,27], and may offer an opportunity for exploring thermoelectric science and technologies at ultralow temperatures, a key environment in quantum information science.

In contrast to the intense research on SSEs, the spin Peltier effect [28–39], the reciprocal of the SSE, remains to be explored at low temperatures below 100 K because of its experimental difficulty. The SPE modulates the temperature of a junction consisting of a metallic film and a magnet in response to a spin current [29], and has been detected usually by means of lock-in thermography (LIT) [29,30,32,36] and thermocouples [28,31,34]. The LIT measures the infrared intensity emitted from the sample surface based on a combination of the lock in with temperature-imaging technique, whose intensity is in proportion to the fourth power of the absolute temperature T (the Stefan-Boltzmann law [32,38]). This results in a typical resolution of 0.1 mK at room temperature [38], which is sufficient to measure a SPE in a prototypical Pt/$Y_3Fe_5O_{12}$ (YIG) system at higher temperatures approximately room temperature and above) [29,30]. However, the LIT may not be applicable for detecting the low-temperature SPE, because its sensitivity is dramatically reduced with decreasing temperature [32,38]. Furthermore, a thermocouple microsensor with a high resolution of approximately 5 μK was used to measure a SPE down to 100 K in Ref. [34]. However, it was found to be difficult to conduct the measurements below 100 K as the

---

[*] t.kikkawa@ap.t.u-tokyo.ac.jp

© 2023 American Physical Society

sensitivity of the thermocouple decreases with decreasing T. It is therefore useful to establish an alternative experimental method for detecting cryogenic SPEs [4]. An ultimate goal in this direction would be to find cryogenic SPEs driven by nuclear and quantum spins that can be activated even at ultralow temperatures, toward future possible cooling- and heat-pump technologies in such an environment.

In this study, we have explored the SPE at a cryogenic temperature below the liquid-^{4}He temperature in a prototypical Pt/YIG system. There are three crucial requirements for practical realization of such measurements that are (1) the high temperature resolution of approximately sub-μK-order or better at low temperatures, (2) ability to detect a temperature change of a metallic (Pt) thin film (which implies for contact-mode measurements sufficient thermal coupling and low heat capacity), and (3) reliability under a high magnetic field environment. To realize the thermometry that meets these requirements, we adopted a RuO_2-based microthermometer [40–49] (RuO_2-AlO_x composite film in our case). In general, RuO_2-based resistors show a high temperature sensitivity due to their large negative temperature coefficient of resistance. Besides, they show reasonably small magnetoresistance and can be made in a thin-film form. Owing to these advantages, in fact, RuO_2-based chip resistors have widely been used as temperature sensors at cryogenic temperatures [40,41]. We have fabricated RuO_2-AlO_x films by means of a co-sputtering technique and found the optimal fabrication condition by characterizing their electric transport properties. By using a RuO_2-AlO_x film as an on-chip temperature sensor for a Pt-film/YIG-slab system, we successfully measured a SPE-induced temperature change on the order of sub-μK at $T = 2$ K. Our results provide a key step toward a complete physical picture of the SPE and establishment of cryogenic spin(calori)tronics [37].

II. EXPERIMENTAL PROCEDURE

A. Fabrication of RuO_2-AlO_x films

We have fabricated RuO_2-AlO_x composite films as a microthermometer by means of dc co-sputtering technique from RuO_2 (99.9%, 2-inch diameter) and Al (99.999%, 2-inch diameter) targets under Ar and O_2 atmosphere. To obtain the most suitable thermometer film for the SPE at low temperatures, a series of co-sputtered RuO_2-AlO_x films on thermally oxidized Si substrates was first prepared at several dc power values for the RuO_2 target ($P_{RuO_2} = 25$, 26, 27, 28, and 30 W) and the fixed dc power for the Al target ($P_{AlO_x} = 25$ W) under a sputtering gas of Ar + 7.83 vol.% O_2 at a pressure of 0.13 Pa at room temperature. Here, the values of Ar-O_2 gas amount and the dc power of $P_{AlO_x} = 25$ W were chosen such that highly insulating AlO_x films are obtained with a reasonable deposition rate (approximately 1 nm/min) when AlO_x is sputtered solely from the Al target. We note that, if the O_2 gas amount exceeds an onset value, the dc sputtering rate suddenly decreases due to the surface oxidization of the Al target [50,51], whereas if the O_2 gas amount is insufficient, the resultant AlO_x film may show finite electrical conduction. We found that the introduction of O_2 by itself does not play a significant role in the temperature variation of the resistance for pure RuO_2 films (for details, see Appendix A). To keep the sputtering conditions and resultant films' quality as consistent as possible through repeated deposition cycles, we introduced common presputtering processes just before actual depositions. To remove a possible oxidized top layer of the Al target, it was presputtered at a relatively high power of $P_{AlO_x} = 30$ W for 600 s without introducing O_2 gas, and then the RuO_2 and Al targets were presputtered for 60 s under the actual deposition conditions (i.e., Ar + 7.83 vol.% O_2) [52]. For electric transport measurements of the RuO_2-AlO_x films, they were patterned into a Hall-bar shape having the length, width, and thickness of 1.0 mm, 0.5 mm, and approximately 100 nm, respectively, by co-sputtering RuO_2-AlO_x through a metal mask. The RuO_2 content in the RuO_2-AlO_x films under the different RuO_2 sputtering power P_{RuO_2} was evaluated through scanning electron microscopy with energy dispersive x-ray analysis (SEM EDX) and the surface roughness of the films was characterized through atomic force microscopy (AFM).

B. Fabrication of SPE device

To investigate the SPE below the liquid-^{4}He temperature, we have prepared devices consisting of a Pt-film/YIG-slab bilayer, where a 100-nm-thick RuO_2-AlO_x film with Au/Ti electrodes is attached on the top surface of the Pt film to detect its SPE-induced temperature change ΔT [see the schematic illustrations and the optical microscope image of a typical SPE device shown in Figs. 1(a)–1(c)]. Three photolithography steps were employed to make the SPE devices, where all the film depositions were performed at room temperature. First, a 5-nm-thick Pt wire with the width of 200 μm was formed on the (111) surface of a single-crystal YIG slab with the size of $5 \times 5 \times 1$ mm^3 by dc magnetron sputtering in a 0.1-Pa Ar atmosphere under the dc power of 20 W. In the next photolithography step, a 70-nm-thick insulating AlO_x layer was formed at the area of 230×350 μm^2 [300×500 μm^2 for the device shown in Fig. 1(c)] on top of the Pt/YIG layer to electrically isolate the RuO_2-AlO_x film from the Pt layer. Here, the AlO_x deposition was done by rf magnetron sputtering from an Al_2O_3 target (99.99%, 2-inch diameter) under the rf power of 150 W and a sputtering gas of Ar + 1.0 vol.% O_2 [53] at a pressure of 0.6 Pa. We later confirmed that the AlO_x film shows a high electric resistance on the order of $1 - 10$ GΩ along the out-of-plane direction at room temperature. Subsequently, a

100-nm-thick RuO_2-AlO_x thermometer film was deposited on top of the AlO_x layer at the area of $230 \times 350\ \mu m^2$ [$300 \times 500\ \mu m^2$ for the device shown in Fig. 1(c)] through the co-sputtering under the dc sputtering power of $P_{RuO_2} = 28$ W and $P_{AlO_x} = 25$ W. Here, the dimensions and sputtering power for the RuO_2-AlO_x film were chosen such that the resistance R of the resulting film is several tens of kΩ at 2 K and its sensitivity monotonically increases with decreasing T down to 2 K [54] [as shown in Figs. 3 and 4(d) and discussed in Sec. III A]. We then proceeded with the final photolithography step for Au(150 nm)/Ti(20 nm) electrodes, where the numbers in parentheses represent the thicknesses of the deposited films. Each Au/Ti electrode wire on the RuO_2-AlO_x film has the 30-μm width and is placed at 50-μm intervals. To reduce the contact resistance between the RuO_2-AlO_x and Ti films, Ar-ion milling was performed directly before depositing the Au/Ti film. Both the Ti and Au layers were formed by rf magnetron sputtering in succession without breaking vacuum. The first lithography process for the Pt layer was done using a single-layer photoresist (AZ5214E) followed by a lift-off process, whereas the second and third processes for the AlO_x/RuO_2-AlO_x and Au/Ti layers were done using a double-layered photoresist (LOR-3A and AZ5214E) to provide an undercut structure for a better success rate of the lift-off process.

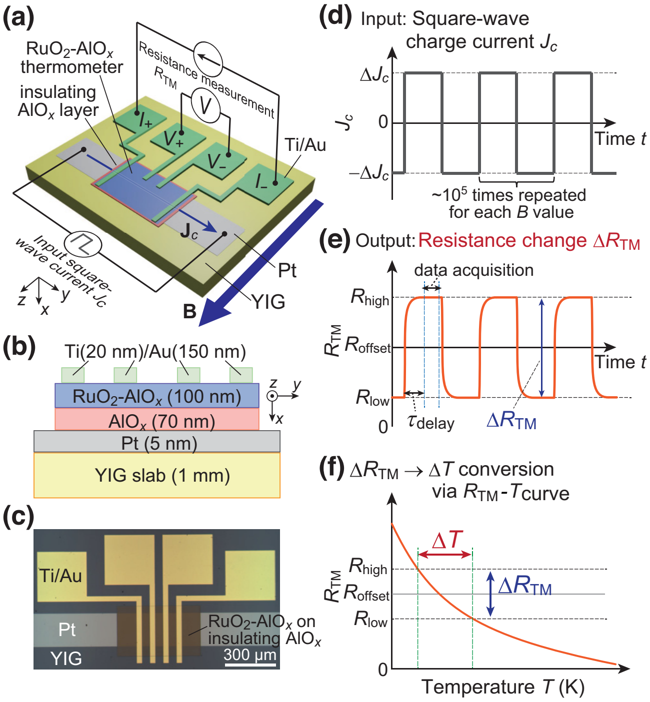

FIG. 1. (a) A schematic illustration of the SPE device consisting of a Pt-film/YIG-slab bilayer, on top of which a RuO_2-AlO_x thermometer (TM) film is attached for the detection of the SPE-induced temperature change ΔT in the Pt film. Besides, in this device, Au/Ti electrodes are formed on the RuO_2-AlO_x film for the four terminal resistance measurements and an AlO_x film is inserted between the RuO_2-AlO_x and Pt films for the electrical insulation between them. (b) A schematic side-view image of the SPE device, where the numbers in parentheses represent the thickness. (c) An optical microscope image of a typical SPE device. (d) Input signal: a square-wave charge current J_c with amplitude ΔJ_c applied to the Pt film. (e) Output signal: a resistance R_{TM} in the RuO_2-AlO_x film that responds to the change in the J_c polarity, $\Delta R_{TM} (\equiv R_{high} - R_{low})$ originating from the SPE-induced ΔT of the Pt film ($\propto \Delta J_c$) [31,34]. Here, the Joule-heating-induced temperature change ($\propto \Delta J_c^2$) is constant in time, and does not overlap with ΔR_{TM}. (f) A schematic illustration of the temperature T dependence of R_{TM}, from which the ΔR_{TM} value can be converted to the temperature change ΔT.

C. SPE and SSE measurements

Figure 1(a) shows a schematic illustration of the SPE device and the experimental setup in the present study. The SPE appears as a result of the interfacial spin and energy transfer between magnons in YIG and electron spins in Pt [28–31]. Suppose that the magnetization $\mathbf{M}$ of the YIG layer is oriented along the $+\hat{\mathbf{z}}$ direction by the external magnetic field $\mathbf{B} \,||\, +\hat{\mathbf{z}}$, as shown in Fig. 1(a). With the application of a charge current $\mathbf{J}_c = J_c\hat{\mathbf{y}}$ to the Pt film, the spin Hall effect (SHE) [55,56] induces a nonequilibrium spin, or magnetic moment, accumulation at the Pt/YIG interface [28–31,34]. For $\mathbf{J}_c \,||\, +\hat{\mathbf{y}}$ ($\mathbf{J}_c \,||\, -\hat{\mathbf{y}}$), the accumulated magnetic moment $\delta\mathbf{m}_s$ at the interfacial Pt orients along the $-\hat{\mathbf{z}}$ ($+\hat{\mathbf{z}}$) direction [30,57], which is antiparallel (parallel) to the $\mathbf{M}$ direction in Fig. 1(a). Through the interfacial spin-flip scattering, $\delta\mathbf{m}_s$ creates or annihilates a magnon in YIG; the number of magnons in YIG increases (decreases) when $\delta\mathbf{m}_s \,||\, -\mathbf{M}$ ($\delta\mathbf{m}_s \,||\, \mathbf{M}$) [4,37]. Because of energy conservation, this process is accompanied by a heat flow $\mathbf{J}_q$ between the electron in Pt and the magnon in YIG [4,37]. The temperature of Pt (YIG) thus decreases (increases) when $\delta\mathbf{m}_s \,||\, -\mathbf{M}$ under $\mathbf{J}_c \,||\, +\hat{\mathbf{y}}$ and $\mathbf{B} \,||\, +\hat{\mathbf{z}}$ [Fig. 1(a)], whereas the temperature of Pt (YIG) increases (decreases) when $\delta\mathbf{m}_s \,||\, \mathbf{M}$ by reversing either $\mathbf{J}_c$ or $\mathbf{B}$ in Fig. 1(a) [29–31,34]. The SPE-induced temperature change ΔT satisfies the following relationship [29–31]:

$$\Delta T \propto \delta\mathbf{m}_s \cdot \mathbf{M} \propto (\mathbf{J}_c \times \mathbf{M}) \cdot \hat{\mathbf{x}}. \tag{1}$$

For the electric SPE detection based on the on-chip thermometer (TM), we utilized the highly accurate resistance measurement scheme called the Delta mode, a combination of low-noise current source and nanovoltmeter (Keithley Model 6221 and 2182A [31,34]). We applied a square-wave charge current J_c with amplitude ΔJ_c to the Pt film [Figs. 1(a) and 1(d)] and measured the four-terminal RuO_2-AlO_x resistance R_{TM} that responds to the change in the J_c polarity, $\Delta R_{TM} \equiv R_{high} - R_{low}$, where R_{high} (R_{low}) represents the R_{TM} value for $J_c = +\Delta J_c$ ($-\Delta J_c$) and was measured under the sensing current of 100 nA applied to the RuO_2-AlO_x film [see Figs. 1(a) and 1(e)] [31]. Here, the ΔR_{TM} value is free from the Joule-heating-induced resistance change ($\propto \Delta J_c^2$) that is independent of time, which thereby contributes only to the offset resistance R_{offset} of the RuO_2-AlO_x film shown in Fig. 1(e) [58]. During the SPE measurement, the magnetic field $\mathbf{B}$ (with magnitude B) was applied in the film plane and perpendicular to the Pt wire, i.e., $\mathbf{B} \,||\, \hat{\mathbf{z}}$ in Fig. 1(a), except for the control experiment shown in Fig. 4(b), where $\mathbf{B} \,||\, \hat{\mathbf{x}}$. The resistance $R_{high,low}$ was recorded after the time delay τ_{delay} of 50 ms [except for the τ_{delay} dependence shown in Fig. 4(e)] during the data-acquisition time τ_{sens} of 20 ms [59], and then was accumulated by repeating the process of the J_c-polarity change approximately 10^5 times for each B point [see Fig. 1(d)] to improve the signal-to-noise ratio. ΔR_{TM} can be converted into the corresponding temperature change $\Delta T (= \Delta R_{TM}/S)$ by using the sensitivity $S \equiv |dR_{TM}/dT|$ of the RuO_2-AlO_x film [see Figs. 1(f) and 4(d)].

To compare the B dependence of the SPE signal with that of the SSE, we also measured the SSE at $T = 2$ K using the same device, for which all SPE results presented in this paper were obtained, but in a different experimental run from the SPE measurement. Here, the SSE measurement was done by means of a lock-in detection technique [19,22,27] and the RuO_2-AlO_x layer was used as a resistive heater; an ac charge current $I_c = \sqrt{2} I_{rms} \sin(\omega t)$ with the amplitude of $I_{rms} = 5.48$ μA and the frequency of $\omega/2\pi = 13.423$ Hz was applied to the RuO_2-AlO_x film, and the second-harmonic voltage in the Pt layer induced by a spin current (driven by a heat current due to the Joule heating of the RuO_2-AlO_x film $P_{heater} = R_{TM} I_{rms}^2$) was detected. During the SSE measurement, the external field $\mathbf{B}$ was applied in the film plane and perpendicular to the Pt wire, i.e., $\mathbf{B} \,||\, \hat{\mathbf{z}}$ in Fig. 1(a).

III. RESULTS AND DISCUSSION

A. Electrical conduction in RuO_2-AlO_x films

We first characterize the electrical conduction of the RuO_2-AlO_x films on thermally oxidized Si substrates. Figure 2(a) shows the T dependence of the resistivity ρ for the films grown under the several (fixed) sputtering power values for the RuO_2 (Al) target P_{RuO_2} (P_{AlO_x}). For all the films, ρ increases with decreasing T in the entire temperature range, showing a negative temperature coefficient of resistance (TCR). Both ρ and its slope $|d\rho/dT|$ increase significantly at low temperatures and monotonically by decreasing the RuO_2 sputtering power P_{RuO_2}. The overall ρ-T curve shifts toward the upper right by decreasing P_{RuO_2}. The result shows that the ρ versus T characteristics of the RuO_2-AlO_x films can be controlled simply by changing the sputtering power P_{RuO_2}. SEM EDX analysis reveals that the RuO_2/AlO_x ratio decreases by decreasing P_{RuO_2} [Fig. 2(c)], which leads to the ρ increase in the electric transport. We also characterized the RuO_2-AlO_x films by means of AFM and found that a typical root-mean-squared surface roughness is $R_{rms} \sim 1$ nm, much smaller than their thickness approximately 100 nm [see the AFM image of the RuO_2-AlO_x films grown under $P_{RuO_2} = 28$ W and $P_{AlO_x} = 25$ W (the RuO_2 content of 41%) shown in Fig. 2(d)].

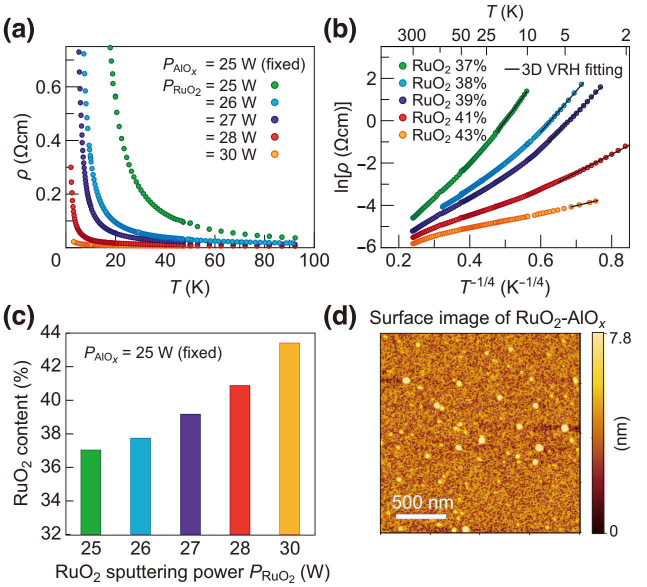

FIG. 2. (a) T dependence of the resistivity ρ for the RuO_2-AlO_x films fabricated on thermally oxidized Si substrates under the several dc sputtering power for the RuO_2 target (P_{RuO_2}) and the fixed dc power for the Al target (P_{AlO_x}). (b) lnρ versus $T^{-1/4}$ for the RuO_2-AlO_x films. The black solid lines are obtained by fitting Eq. (2) (the 3D Mott VRH model) to the experimental data. (c) Relationship between the RuO_2 content in the RuO_2-AlO_x films and the RuO_2 sputtering power P_{RuO_2} determined by SEM EDX. Using this correspondence, the figure legends in (b) and also Fig. 3 are described in terms of the RuO_2 content. (d) A typical AFM image of the RuO_2-AlO_x film grown under $P_{RuO_2} = 28$ W and $P_{AlO_x} = 25$ W (the RuO_2 content of 41%), where the root-mean-squared surface roughness is $R_{rms} = 1.2$ nm. The white scale bar represents 500 nm.

The electrical conduction at sufficiently low temperatures for RuO_2-based thermometers has often been analyzed by the variable-range hopping (VRH) model for three-dimensional (3D) systems proposed by Mott [41–46, 60,61],

$$\rho = \rho_0 \exp\left(\frac{T_0}{T}\right)^{1/4}, \tag{2}$$

where ρ_0 is the resistivity coefficient and T_0 is the characteristic temperature related to the electron localization length a. To discuss our result in light of the VRH, we plot lnρ versus $T^{-1/4}$ for the RuO_2-AlO_x films in Fig. 2(b). We found that lnρ scales linearly with $T^{-1/4}$ at low-T ranges,

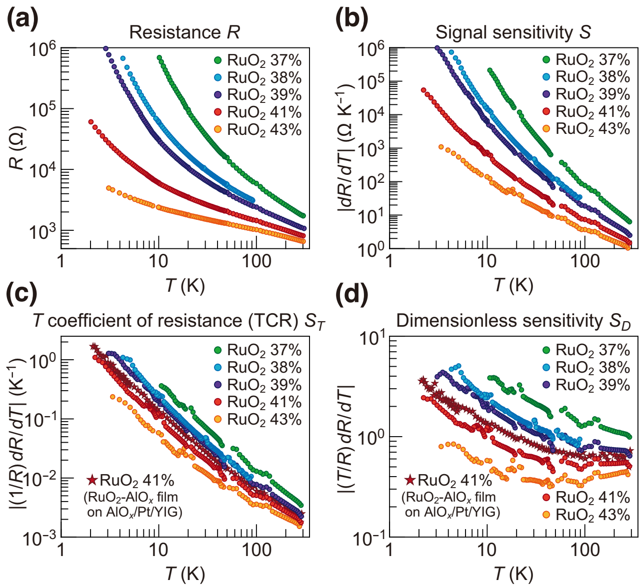

FIG. 3. T dependence of (a) the resistance R, (b) the sensitivity $S \equiv |dR/dT|$, (c) the temperature coefficient of resistance (TCR) $S_T \equiv |(1/R)dR/dT|$, and (d) the dimensionless sensitivity $S_D \equiv |(T/R)dR/dT| = |d(\ln R)/d(\ln T)|$ for the RuO$_2$-AlO$_x$ films with different RuO$_2$ content fabricated on thermally oxidized Si substrates. The films are patterned into a Hall-bar shape having the length, width, and thickness of 1.0 mm, 0.5 mm, and approximately 100 nm, respectively, by co-sputtering RuO$_2$-AlO$_x$ through a metal mask. In (c) and (d), the $S_T(T)$ and $S_D(T)$ results for the RuO$_2$-AlO$_x$ thermometer film on the Pt/YIG sample are coplotted (red star marks).

and the lnρ–$T^{-1/4}$ data is well fitted by Eq. (2) [see the black solid lines in Fig. 2(b)], suggesting that the low-T electrical conduction is indeed governed by the VRH. From the fitting, the T_0 values are obtained as 2.58×10^5, 1.41×10^5, 8.95×10^4, 5.73×10^3, and 2.60×10^2 K for the RuO$_2$-AlO$_x$ films grown under $P_{\mathrm{RuO_2}} = 25$, 26, 27, 28, and 30 W, respectively. We note that, at all the T ranges adopted for the VRH fitting, the average hopping distance (R_{hop}) is larger than the electron localization length (a) that is the requirement for the VRH model to be valid: $R_{\mathrm{hop}}/a = (3/8)(T_0/T)^{1/4} > 1$ [62–66]. Besides, the Mott hopping energy $E_{\mathrm{hop}} = (1/4)k_BT(T_0/T)^{1/4}$ (k_B is the Boltzmann constant) obtained for the present films is larger than (or comparable to) the thermal energy k_BT, allowing for the electron hopping [62–66]. The above argument further confirms the validity of the 3D Mott VRH model to describe the conduction mechanism in the RuO$_2$-AlO$_x$ films.

We here discuss the T-dependent thermometer characteristics of the RuO$_2$-AlO$_x$ films. Figure 3 shows the T dependence of (a) the resistance R, (b) the sensitivity $S \equiv |dR/dT|$, (c) the temperature coefficient of resistance (TCR) $S_T \equiv |(1/R)dR/dT|$, and (d) the dimensionless sensitivity $S_D \equiv |(T/R)dR/dT| = |d(\ln R)/d(\ln T)|$ for the RuO$_2$-AlO$_x$ films. Here, the sensitivity S is an essential quantity when the thermometer is used as an actual temperature-sensor device in its original form. The TCR S_T is the normalized sensitivity S by the measured resistance R, given that S is geometry dependent (i.e., dR/dT scales with R) [40]. The dimensionless sensitivity S_D is a measure often used to compare the performance of the thermometers made of different materials, regardless of their size [40,67–69]. For the present RuO$_2$-AlO$_x$ films with low RuO$_2$ content ($<$ 40%), the sensitivity S takes a high value on the order of $10^4 - 10^6$ Ω/K below $T \sim 10$ K. For such a low-T range, however, their resistance R values are highly enhanced, and exceed 1 MΩ at 2 K, which is too high to use such films as thermometers in their original dimensions below the liquid-^{4}He temperature. Besides, their TCR values start to show a saturation behavior by decreasing T in such a low-T environment. By contrast, the RuO$_2$-AlO$_x$ film with the RuO$_2$ content of 41% (fabricated under $P_{\mathrm{RuO_2}} = 28$ W and $P_{\mathrm{AlO}_x} = 25$ W) shows a moderate R (S) value of $10^4 - 10^5$ Ω ($10^4 - 10^5$ Ω/K) and the best TCR characteristic of approximately 100% K^{-1} around 2 K. We therefore adopt its growth condition for our SPE device. Overall, the S, TCR, and S_D values of the present RuO$_2$-AlO$_x$ films are comparable to those of commercially available Cernox$^{\mathrm{TM}}$ zirconium oxy-nitride sensors [40,69], carbon composites [41,70,71], and AuGe films [68] commonly used at a similar T range.

B. Observation of SPE based on RuO$_2$-AlO$_x$ on-chip thermometer

We are now in a position to demonstrate a cryogenic SPE in the Pt/YIG sample based on the RuO$_2$-AlO$_x$ on-chip thermometer. Figure 4(a) shows the B dependence of the RuO$_2$-AlO$_x$ resistance change ΔR_{TM} measured at $T = 2$ K and a low-B range of $|B| \leq 0.2$ T. With the application of the charge current $\Delta J_c (= 0.15$ mA) to the Pt film, a clear ΔR_{TM} signal appears with a magnitude saturated at approximately 30 mΩ [73] and its sign changes depending on the $\mathbf{B}$ ($|| \pm \hat{\mathbf{z}}$) direction. The signal disappears either when ΔJ_c is essentially zero [gray diamonds in Fig. 4(a)] or when $\mathbf{B}$ is applied perpendicular to the Pt/YIG interface ($\mathbf{B} \, || \pm \hat{\mathbf{x}}$) [Fig. 4(b)]. We also confirmed that the B dependence of ΔR_{TM} is consistent with that of the SSE in the identical Pt/YIG device [see Fig. 4(c)]. These are the representative features of the SPE [29–38]. Furthermore, the sign of ΔR_{TM} agrees with the SPE-induced temperature change [29,30]. As shown in Fig. 4(a), the measured ΔR_{TM} value is positive for $B > 0$, meaning that the resistance R_{TM} increases (decreases) when $\mathbf{J}_c \, || + \hat{\mathbf{y}}$ ($\mathbf{J}_c \, || - \hat{\mathbf{y}}$), for which the orientation of the SHE-induced magnetic moment at the interfacial Pt layer is $\delta\mathbf{m}_s \, || - \hat{\mathbf{z}}$ ($\delta\mathbf{m}_s \, || + \hat{\mathbf{z}}$) in Fig. 1(a). According to the negative TCR of the RuO$_2$-AlO$_x$ film, this implies that the temperature of the Pt film decreases (increases) when $\delta\mathbf{m}_s \, || - \hat{\mathbf{z}}$ ($\delta\mathbf{m}_s \, || +$

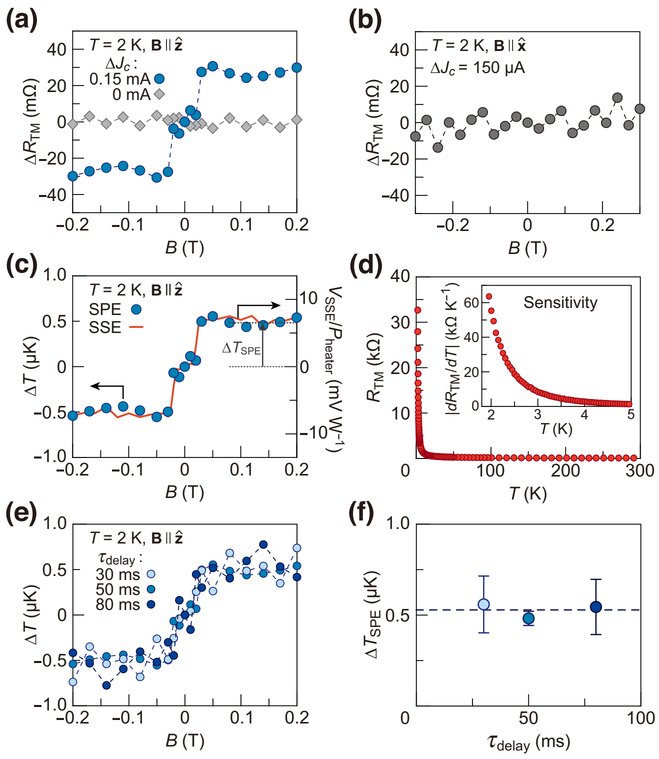

FIG. 4. (a) B dependence of the SPE-induced ΔR_{TM} at $T=2$ K and $B \leq 0.2$ T ($\mathbf{B}\,||\,\hat{\mathbf{z}}$) under $\Delta J_c = 0.15$ and 0.00 mA and $\tau_{\mathrm{delay}} = 50$ ms. The dashed lines connect adjacent plots. (b) B dependence of ΔR_{TM} for $\mathbf{B}\,||\,\hat{\mathbf{x}}$ ($B \leq 0.3$ T) under $\Delta J_c = 0.15$ mA. Note that the applied B is larger than the out-of-plane ($\mathbf{B}\,||\,\hat{\mathbf{x}}$) saturation field for bulk YIG, which is approximately 0.2 T [72]. (c) Comparison between the B dependence of the SPE-induced temperature change ΔT (blue filled circles) and the SSE-induced voltage normalized by heating power $V_{\mathrm{SSE}}/P_{\mathrm{heater}}$ (orange solid curve) at $T = 2$ K and $\mathbf{B}\,||\,\hat{\mathbf{z}}$. The SPE data shown here is the same as that plotted in (a), but the left vertical axis is converted from ΔR_{TM} to ΔT via the R_{TM}-T calibration curve plotted in (d). For details of the SSE measurement, see Sec. II C. (d) T dependence of R_{TM} (main) and $|dR_{\mathrm{TM}}/dT|$ (inset) for the RuO$_2$-AlO$_x$ film on the Pt/YIG sample. (e) B dependence of the SPE-induced ΔT at $T = 2$ K under $\Delta J_c = 0.15$ mA and several τ_{delay} values. (f) τ_{delay} dependence of the magnitude of the SPE-induced temperature change ΔT_{SPE}, where ΔT_{SPE} is evaluated by averaging the ΔT values for 0.08 T $\leq B \leq$ 0.2 T [see also (c)]. The dashed line represents the averaged value. All the ΔR_{TM} and ΔT data were antisymmetrized with respect to the magnetic field B.

$\hat{\mathbf{z}}$) under $\mathbf{M}\,||\,\mathbf{B}\,||+\hat{\mathbf{z}}$. This correspondence between the sign of the temperature change ΔT and the relative orientation of $\delta\mathbf{m}_s$ with respect to $\mathbf{M}$ is consistent with the scenario of the SPE described in Sec. II C. We thus conclude that we succeeded in measuring a cryogenic SPE using the RuO$_2$-AlO$_x$ on-chip thermometer film.

To convert the ΔR_{TM} value to the temperature change ΔT, we measured the R_{TM}-T curve for the RuO$_2$-AlO$_x$ film. As shown in Fig. 4(d), similar to the results described in Sec. III A, its resistance R_{TM} increases dramatically with decreasing T at low temperatures, and the sensitivity $S = |dR_{\mathrm{TM}}/dT|$ is as large as 55.3 kΩ/K at 2 K. [The TCR S_T and dimensionless sensitivity S_D for the film are plotted in Figs. 3(c) and 3(d), respectively, and ρ and $|d\rho/dT|$ are plotted in Figs. 7(a) and 7(b) in Appendix B, respectively, together with the results for the RuO$_2$-AlO$_x$ films grown on thermally oxidized Si substrates.] In Fig. 4(c), we replot the B dependence of the SPE in units of the temperature change ΔT ($= \Delta R_{\mathrm{TM}}/S$) using the above S value. We evaluate the magnitude of the SPE-induced temperature change to be $\Delta T_{\mathrm{SPE}} = 482 \pm 39$ nK, by averaging the ΔT values for 0.08 T $\leq B \leq$ 0.2 T, at which the magnetization $\mathbf{M}$ of the YIG slab fully orients along the $\mathbf{B}$ direction [74] [see the dashed line in Fig. 4(c)]. The standard deviation of 39 nK shows that our measurement scheme based on the RuO$_2$-AlO$_x$ on-chip thermometer can resolve an extremely small ΔT on the order of several tens of nK (which is a value achieved by repeating the process of the J_c-polarity change of 7×10^4 times at each B). The ΔT resolution is much higher than that reported in the previous SPE measurements based on lock-in thermography, lock-in thermoreflectance, and thermocouples, for which the typical resolution is 100, 10 − 100, and 5 μK, respectively [34,38,39]. We found that the magnitude of ΔT_{SPE} normalized by the charge-current density Δj_c applied to the Pt wire is $\Delta T_{\mathrm{SPE}}/\Delta j_c = 3.2 \times 10^{-15}$ Km^2/A, which is 2 orders of magnitude smaller than the corresponding value for Pt/YIG systems measured at room temperature [30,31]. The low-T signal reduction of the SPE is consistent with that found in the SSE [17,75–77], and is attributed mainly to the reduction of the thermally activated magnons contributing to these phenomena at cryogenic temperatures. Besides, there can be a finite-temperature gradient across the insulating AlO$_x$ film, between the Pt and RuO$_2$-AlO$_x$ layers, resulting in a further decrease of the detected ΔT signal. We also measured the delay time τ_{delay} dependence of the SPE and found that the ΔT_{SPE} takes almost the same value in the present τ_{delay} range (30 ms $\leq \tau_{\mathrm{delay}} \leq$ 80 ms) [see Figs. 4(e) and 4(f)], showing that all the data were obtained under the steady-state condition [31,35].

We also explored the high magnetic field response of the SPE signal. Figure 5(a) displays the ΔT versus B data measured at $T = 2$ K and $B \leq 10$ T ($\mathbf{B}\,||\,\hat{\mathbf{z}}$). We found that ΔT exhibits a maximum at a low B ($\lesssim 0.2$ T) and, by increasing B, gradually decreases and is eventually suppressed. The B dependence of the SPE agrees well with that of the SSE measured with the identical device [see Fig. 5(a)]. We note that the magnetoresistance (MR) ratio of the RuO$_2$-AlO$_x$ film is as small as approximately 3.7% for $B \leq 10$ T at $T = 2$ K, so that the device can be used reliably under the high-B range. The observed $\Delta T\,(B)$ feature is explained in terms of the suppression of magnon excitations by the Zeeman effect, as established in the previous SSE research [17,27,75–77] [see Fig. 5(b)]. By increasing

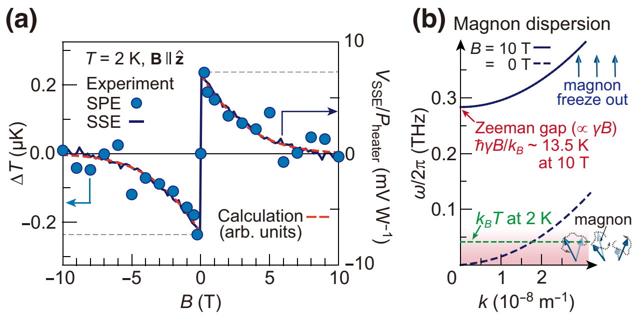

FIG. 5. (a) Comparison between the high magnetic field B response of the SPE-induced temperature change ΔT (blue filled circles) and the SSE-induced voltage normalized by heating power $V_{\mathrm{SSE}}/P_{\mathrm{heater}}$ (blue solid curve) at $T = 2$ K and $B \leq 10$ T ($\mathbf{B} \,||\, \hat{\mathbf{z}}$). The SPE data was obtained under $\Delta J_c = 0.15$ mA and $\tau_{\mathrm{delay}} = 50$ ms. For details of the SSE measurement, see Sec. II C. The orange dashed curve shows the numerically calculated result based on Eq. (3) for $T = 2$ K. (b) Magnon dispersion relations for YIG [15] at $B = 0$ and 10 T, at which the magnon-excitation gap values are approximately 0 and 13.5 K in units of temperature, respectively, where k represents the wave number. The thermal energy ($k_B T$) level of 2 K is also plotted with a green dashed line, above which thermal excitation is exponentially suppressed.

B, the magnon dispersion shifts toward high frequencies due to the Zeeman interaction ($\propto \gamma B$). At $B = 10$ T, the Zeeman energy $\hbar\gamma B$ is approximately 13.5 K in units of temperature, which is greater than the thermal energy $k_B T$ at 2 K [see Fig. 5(b)], resulting in an insignificant value of the Boltzmann factor: $\exp(-\hbar\gamma B/k_B T) \sim 10^{-3} \ll 1$, where γ and $\hbar$ represent the gyromagnetic ratio and Dirac constant, respectively. Therefore, the thermal magnons that can contribute to the SPE at a low B are gradually suppressed with the increase of B and, at $B \sim 10$ T, are hardly excited by the strong Zeeman gap in the magnon spectrum [Fig. 5(b)], which leads to the suppression of the SPE in the low-T and high-B environment. We also compared the experimental result with a calculation for the interfacial heat current induced by the SPE J_q^{SPE} and spin current induced by the SSE J_s^{SSE}, which are expressed as

$$
\begin{aligned}
J_q^{\mathrm{SPE}} &\propto \int \frac{d^3k}{(2\pi)^3}\, \omega^2 \frac{\partial n_{\mathrm{BE}}}{\partial \omega}, \\
J_s^{\mathrm{SSE}} &\propto -\int \frac{d^3k}{(2\pi)^3}\, \omega T \frac{\partial n_{\mathrm{BE}}}{\partial T},
\end{aligned}
\tag{3}
$$

respectively [75,78–81]. Here, $\omega = D_{\mathrm{ex}}k^2 + \gamma B$ is the parabolic magnon dispersion for YIG with the stiffness constant of $D_{\mathrm{ex}} = 7.7 \times 10^{-6}$ m^2/s [15] and $n_{\mathrm{BE}} = [\exp(\hbar\omega/k_B T) - 1]^{-1}$ is the Bose-Einstein distribution function. Note that the relation $\omega \partial n_{\mathrm{BE}}/\partial\omega = -T \partial n_{\mathrm{BE}}/\partial T$ ensures the Onsager reciprocity between the SSE and SPE [81], which makes the above expressions to be of the same form in terms of the B dependence. As shown by the orange dashed curve in Fig. 5(a), the calculated result based on Eq. (3) well reproduces the experiment. This result further supports the origin of the measured ΔT signal and provides additional clues for further understanding of the physics of the SPE.

IV. CONCLUSIONS

In this study, we have fabricated RuO$_2$-AlO$_x$ films by means of a dc co-sputtering technique and characterized their electrical conduction and sensitivity at low temperatures. The sensitivity was found to be tuned simply by the relative sputtering power applied for the RuO$_2$ and Al targets, and the TCR value reaches approximately 100% K^{-1} for the RuO$_2$-AlO$_x$ films with the moderate RuO$_2$ content ($\gtrsim$41%). By using the RuO$_2$-AlO$_x$ film as an on-chip microthermometer, we successfully measured the SPE-induced temperature change ΔT in a Pt-film/YIG-slab system at the low temperature of 2 K based on the so-called Delta method, which can resolve an extremely small ΔT value of several tens of nK. We also measured the high B response of the SPE at $T = 2$ K up to $B = 10$ T, and found that, by increasing B, the SPE signal gradually decreases and is eventually suppressed. The B dependence can be interpreted in terms of the field-induced freeze out of magnons due to the Zeeman gap opening in the magnon spectrum of YIG. We anticipate that our experimental methods based on an on-chip thin-film thermometer will be useful for exploring low-T thermoelectric heating and cooling effects in various types of microdevices, including a system based on two-dimensional van der Waals materials [82–84]. Besides, with an appropriate optimization of the resistance and sensitivity of the RuO$_2$-AlO$_x$ films by controlling the content of RuO$_2$, our results can be extended toward even lower temperature ranges below 1 K, where they can be used to detect unexplored cryogenic spin caloritronic effects driven by nuclear and quantum spins.

ACKNOWLEDGMENTS

We thank S. Daimon, R. Yahiro, J. Numata, K.K. Meng, H. Arisawa, T. Makiuchi, and T. Hioki for valuable discussions. This work was supported by JST-CREST (Grants No. JPMJCR20C1 and No. JPMJCR20T2), Grant-in-Aid for Scientific Research (Grants No. JP19H05600, No. JP20H02599, and No. JP22K18686) and Grant-in-Aid for Transformative Research Areas (Grant No. JP22H05114) from JSPS KAKENHI, MEXT Initiative to Establish Next-generation Novel Integrated Circuits Centers (X-NICS) (Grant No. JPJ011438), Japan, Murata Science Foundation, Daikin Industries, Ltd, and Institute for AI and Beyond of the University of Tokyo.

APPENDIX A: ELECTRICAL CONDUCTION IN PURE RuO_2 FILMS

To check the effect of O_2 gas introduction during sputtering on the RuO_2 film, we also fabricated pristine (polycrystalline) RuO_2 films under only Ar gas flow and also under a large amount of O_2 gas flow (Ar + 33.3 vol.% O_2, which is approximately 5 times greater than that used for the RuO_2-AlO_x deposition) and measured their R-T curves. Here, the RuO_2 films were patterned into a Hall-bar shape having the length, width, and thickness of 2.0 mm, 0.3 mm, and approximately 10 nm, respectively, by sputtering RuO_2 through a metal mask. Figure 6 shows the T dependence of R normalized by the value at 300 K for each RuO_2 film. For both the films, the R-T curve shows almost the same characteristics; R gradually increases with decreasing T and the $R(T)/R(300\text{ K})$ value at $T = 2$ K (the temperature of interest) deviates only approximately 2% with each other. This result shows that the effect of oxygen on the RuO_2 deposition does not play an essential role in the R versus T characteristics of RuO_2.

APPENDIX B: COMPARISON OF ρ-T CURVES BETWEEN RuO_2-AlO_x FILMS ON SiO_2/Si SUBSTRATES AND ON Pt/YIG DEVICE

Figures 7(a) and 7(b) show the double logarithmic plot of (a) the resistivity ρ and (b) its slope $|d\rho/dT|$ versus temperature T for the RuO_2-AlO_x films on thermally oxidized Si substrates (filled circles) and on the Pt/YIG sample (red star marks) grown under the several dc sputtering power for the RuO_2 target (P_{RuO_2}) and the fixed dc power for the Al target ($P_{AlO_x} = 25$ W). Although a small deviation of the ρ and $|d\rho/dT|$ values is observed even under the same growth condition depending on the substrate layer (i.e., SiO_2/Si or Pt/YIG), the overall T-dependent feature agrees well with each other. Note that the substrate-dependent difference in the ρ and $|d\rho/dT|$ values does not have a significant impact on the observation of the cryogenic SPE, if the sensitivity is large enough for its detection.

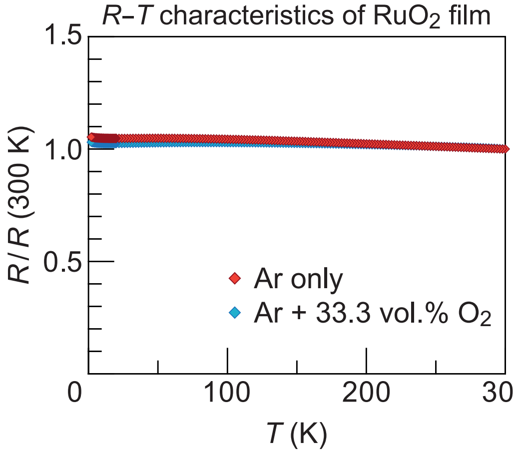

FIG. 6. T dependence of $R/R(T = 300\text{ K})$ for the pure RuO_2 films grown under only Ar gas flow and also under a large amount of O_2 gas flow (Ar + 33.3 vol.% O_2), for which the resistivity ρ values at $T = 300$ K are evaluated as 3.21×10^{-4} and 3.96×10^{-4} Ωcm, respectively.

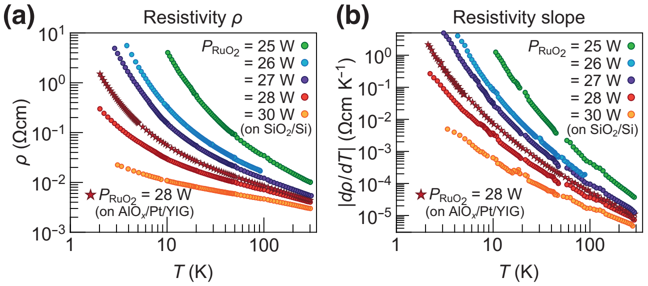

FIG. 7. T dependence of (a) the resistivity ρ and (b) its slope $|d\rho/dT|$ for the RuO_2-AlO_x films on thermally oxidized Si substrates (filled circles) and on the Pt/YIG sample (red star marks) grown under the several dc sputtering power for the RuO_2 target (P_{RuO_2}) and the fixed dc power for the Al target ($P_{AlO_x} = 25$ W). Note that $S_T \equiv |(1/R)dR/dT| = |(1/\rho)d\rho/dT|$ and $S_D \equiv |(T/R)dR/dT| = |(T/\rho)d\rho/dT|$, the T dependences of which are shown in Figs. 3(c) and 3(d), respectively.

[1] H. Ohno, M. D. Stiles, and B. Dieny, Spintronics, Proc. IEEE **104**, 1782 (2016).

[2] A. V. Chumak, P. Kabos, M. Wu, C. Abert, C. Adelmann, A. O. Adeyeye, J. Åkerman, F. G. Aliev, A. Anane, and A. Awad, *et al.*, Advances in magnetics roadmap on spin-wave computing, IEEE Trans. Magn. **58**, 0800172 (2022).

[3] H. Yang, S. O. Valenzuela, M. Chshiev, S. Couet, B. Dieny, B. Dlubak, A. Fert, K. Garello, M. Jamet, D.-E. Jeong, K. Lee, T. Lee, M.-B. Martin, G. S. Kar, P. Sénéor, H.-J. Shin, and S. Roche, Two-dimensional materials prospects for non-volatile spintronic memories, Nature **606**, 663 (2022).

[4] S. Maekawa, T. Kikkawa, H. Chudo, J. Ieda, and E. Saitoh, Spin and spin current–From fundamentals to recent progress, J. Appl. Phys. **133**, 020902 (2023).

[5] Y. Fan, P. Upadhyaya, X. Kou, M. Lang, S. Takei, Z. Wang, J. Tang, L. He, L.-T. Chang, M. Montazeri, G. Yu, W. Jiang, T. Nie, R. N. Schwartz, Y. Tserkovnyak, and K. L. Wang, Magnetization switching through giant spin-orbit torque in a magnetically doped topological insulator heterostructure, Nat. Mater. **13**, 699 (2014).

[6] J. Linder and J. W. A. Robinson, Superconducting spintronics, Nat. Phys. **11**, 307 (2015).

[7] M. Umeda, Y. Shiomi, T. Kikkawa, T. Niizeki, J. Lustikova, S. Takahashi, and E. Saitoh, Spin-current coherence peak in superconductor/magnet junctions, Appl. Phys. Lett. **112**, 232601 (2018).

[8] Y. Yao, Q. Song, Y. Takamura, J. P. Cascales, W. Yuan, Y. Ma, Y. Yun, X. C. Xie, J. S. Moodera, and W. Han, Probe of spin dynamics in superconducting NbN thin films via spin pumping, Phys. Rev. B **97**, 224414 (2018).

[9] Y. Shiomi, J. Lustikova, S. Watanabe, D. Hirobe, S. Takahashi, and E. Saitoh, Spin pumping from nuclear spin waves, Nat. Phys. **15**, 22 (2019).

[10] K.-R. Jeon, J.-C. Jeon, X. Zhou, A. Migliorini, J. Yoon, and S. S. P. Parkin, Giant transition-state quasiparticle spin-Hall effect in an exchange-spin-split superconductor detected by nonlocal magnon spin transport, ACS Nano **14**, 15874 (2020).

[11] C. L. Tschirhart, E. Redekop, L. Li, T. Li, S. Jiang, T. Arp, O. Sheekey, T. Taniguchi, K. Watanabe, M. E. Huber, K. F. Mak, J. Shan, and A. F. Young, Intrinsic spin Hall torque in a moiré Chern magnet, Nat. Phys. **19**, 807 (2023).

[12] K. Uchida, H. Adachi, T. Kikkawa, A. Kirihara, M. Ishida, S. Yorozu, S. Maekawa, and E. Saitoh, Thermoelectric generation based on spin Seebeck effects, Proc. IEEE **104**, 1946 (2016).

[13] S. M. Rezende, *Fundamentals of Magnonics* (Springer Nature Switzerland AG, Switzerland, 2020).

[14] T. Kikkawa and E. Saitoh, Spin Seebeck effect: Sensitive probe for elementary excitation, spin correlation, transport, magnetic order, and domains in solids, Annu. Rev. Condens. Matter Phys. **14**, 129 (2023).

[15] T. Kikkawa, K. Shen, B. Flebus, R. A. Duine, K. Uchida, Z. Qiu, G. E. W. Bauer, and E. Saitoh, Magnon polarons in the spin Seebeck effect, Phys. Rev. Lett. **117**, 207203 (2016).

[16] L. J. Cornelissen, K. Oyanagi, T. Kikkawa, Z. Qiu, T. Kuschel, G. E. W. Bauer, B. J. van Wees, and E. Saitoh, Nonlocal magnon-polaron transport in yttrium iron garnet, Phys. Rev. B **96**, 104441 (2017).

[17] K. Oyanagi, T. Kikkawa, and E. Saitoh, Magnetic field dependence of the nonlocal spin Seebeck effect in Pt/YIG/Pt systems at low temperatures, AIP Adv. **10**, 015031 (2020).

[18] J. Li, H. T. Simensen, D. Reitz, Q. Sun, W. Yuan, C. Li, Y. Tserkovnyak, A. Brataas, and J. Shi, Observation of magnon polarons in a uniaxial antiferromagnetic insulator, Phys. Rev. Lett. **125**, 217201 (2020).

[19] T. Kikkawa, K. Oyanagi, T. Hioki, M. Ishida, Z. Qiu, R. Ramos, Y. Hashimoto, and E. Saitoh, Composition-tunable magnon-polaron anomalies in spin Seebeck effects in epitaxial $\mathrm{Bi}_x\mathrm{Y}_{3-x}\mathrm{Fe}_5\mathrm{O}_{12}$ films, Phys. Rev. Mater. **6**, 104402 (2022).

[20] S. Geprägs, A. Kehlberger, F. D. Coletta, Z. Qiu, E.-J. Guo, T. Schulz, C. Mix, S. Meyer, A. Kamra, M. Althammer, H. Huebl, G. Jakob, Y. Ohnuma, H. Adachi, J. Barker, S. Maekawa, Gerrit E. W. Bauer, E. Saitoh, R. Gross, S. T. B. Goennenwein, and M. Kläui, Origin of the spin Seebeck effect in compensated ferrimagnets, Nat. Commun. **7**, 10452 (2016).

[21] W. Yuan, Q. Zhu, T. Su, Y. Yao, W. Xing, Y. Chen, Y. Ma, X. Lin, J. Shi, R. Shindou, X. C. Xie, and W. Han, Experimental signatures of spin superfluid ground state in canted antiferromagnet $\mathrm{Cr}_2\mathrm{O}_3$ via nonlocalspin transport, Sci. Adv. **4**, eaat1098 (2018).

[22] S. M. Wu, J. E. Pearson, and A. Bhattacharya, Paramagnetic spin Seebeck effect, Phys. Rev. Lett. **114**, 186602 (2015).

[23] K. Oyanagi, S. Takahashi, T. Kikkawa, and E. Saitoh, Mechanism of paramagnetic spin Seebeck effect, Phys. Rev. B **107**, 014423 (2023).

[24] D. Hirobe, M. Sato, T. Kawamata, Y. Shiomi, K. Uchida, R. Iguchi, Y. Koike, S. Maekawa, and E. Saitoh, One-dimensional spinon spin currents, Nat. Phys. **13**, 30 (2017).

[25] Y. Chen, M. Sato, Y. Tang, Y. Shiomi, K. Oyanagi, T. Masuda, Y. Nambu, M. Fujita, and E. Saitoh, Triplon current generation in solids, Nat. Commun. **12**, 5199 (2021).

[26] W. Xing, R. Cai, K. Moriyama, K. Nara, Y. Yao, W. Qiao, K. Yoshimura, and W. Han, Spin Seebeck effect in quantum magnet $\mathrm{Pb}_2\mathrm{V}_3\mathrm{O}_9$, Appl. Phys. Lett. **120**, 042402 (2022).

[27] T. Kikkawa, D. Reitz, H. Ito, T. Makiuchi, T. Sugimoto, K. Tsunekawa, S. Daimon, K. Oyanagi, R. Ramos, S. Takahashi, Y. Shiomi, Y. Tserkovnyak, and E. Saitoh, Observation of nuclear-spin Seebeck effect, Nat. Commun. **12**, 4356 (2021).

[28] J. Flipse, F. K. Dejene, D. Wagenaar, G. E. W. Bauer, J. Ben Youssef, and B. J. van Wees, Observation of the spin Peltier effect for magnetic insulators, Phys. Rev. Lett. **113**, 027601 (2014).

[29] S. Daimon, R. Iguchi, T. Hioki, E. Saitoh, and K. Uchida, Thermal imaging of spin Peltier effect, Nat. Commun. **7**, 13754 (2016).

[30] S. Daimon, K. Uchida, R. Iguchi, T. Hioki, and E. Saitoh, Thermographic measurements of the spin Peltier effect in metal/yttrium-iron-garnet junction systems, Phys. Rev. B **96**, 024424 (2017).

[31] R. Itoh, R. Iguchi, S. Daimon, K. Oyanagi, K. Uchida, and E. Saitoh, Magnetic-field-induced decrease of the spin Peltier effect in $\mathrm{Pt}/\mathrm{Y}_3\mathrm{Fe}_5\mathrm{O}_{12}$ system at room temperature, Phys. Rev. B **96**, 184422 (2017).

[32] A. Yagmur, R. Iguchi, S. Geprägs, A. Erb, S. Daimon, E. Saitoh, R. Gross, and K. Uchida, Lock-in thermography measurements of the spin Peltier effect in a compensated ferrimagnet and its comparison to the spin Seebeck effect, J. Phys. D: Appl. Phys. **51**, 194002 (2018).

[33] A. Sola, V. Basso, M. Kuepferling, C. Dubs, and M. Pasquale, Experimental proof of the reciprocal relation between spin Peltier and spin Seebeck effects in a bulk YIG/Pt bilayer, Sci. Rep. **9**, 2047 (2019).

[34] R. Yahiro, T. Kikkawa, R. Ramos, K. Oyanagi, T. Hioki, S. Daimon, and E. Saitoh, Magnon polarons in the spin Peltier effect, Phys. Rev. B **101**, 024407 (2020).

[35] T. Yamazaki, R. Iguchi, T. Ohkubo, H. Nagano, and K. Uchida, Transient response of the spin Peltier effect revealed by lock-in thermoreflectance measurements, Phys. Rev. B **101**, 020415(R) (2020).

[36] S. Daimon, K. Uchida, N. Ujiie, Y. Hattori, R. Tsuboi, and E. Saitoh, Thickness dependence of spin Peltier effect visualized by thermal imaging technique, Appl. Phys. Express **13**, 103001 (2020).

[37] K. Uchida, Transport phenomena in spin caloritronics, Proc. Jpn. Acad., Ser. B **97**, 69 (2021).

[38] K. Uchida and R. Iguchi, Spintronic thermal management, J. Phys. Soc. Jpn. **90**, 122001 (2021).

[39] A. Takahagi, R. Iguchi, H. Nagano, and K. Uchida, Highly sensitive lock-in thermoreflectance temperature measurement using thermochromic liquid crystal, Appl. Phys. Lett. **122**, 172401 (2023).

[40] Cernox Sensors Catalog, Cryogenic temperature sensor characteristics, Cernox vs. Rox Sensor Performance, in

Temperature Sensor Information, Lake Shore https://www.lakeshore.com/resources/sensors.

[41] F. Pobell, *Matter and Methods at Low Temperatures* (Springer-Verlag Berlin Heidelberg, Heidelberg, 2007).

[42] W. A. Bosch, F. Mathu, H. C. Meijer, and R. W. Willekers, Behaviour of thick film resistors (Philips type RC-01) as low temperature thermometers in magnetic fields up to 5 T, Cryogenics **26**, 3 (1986).

[43] Q. Li, C. H. Watson, R. G. Goodrich, D. G. Haase, and H. Lukefahr, Thick film chip resistors for use as low temperature thermometers, Cryogenics **26**, 467 (1986).

[44] I. Bat'ko, K. Flachbart, M. Somora, and D. Vanický, Design of RuO_2-based thermometers for the millikelvin temperature range, Cryogenics **35**, 105 (1995).

[45] B. Neppert and P. Esquinazi, Temperature and magnetic field dependence of thick-film resistor thermometers (Dale type RC550), Cryogenics **36**, 231 (1996).

[46] M. Affronte, M. Campani, S. Piccinini, M. Tamborin, B. Morten, M. Prudenziati, and O. Laborde, Low temperature electronic transport in RuO_2-based cermet resistors, J. Low Temp. Phys. **109**, 461 (1997).

[47] Y.-Y. Chen, Low-temperature Ru-sapphire film thermometer and its application in heat capacity measurements, AIP Conf. Proc. **684**, 387 (2003).

[48] Y. Y. Chen, P. C. Chen, C. B. Tsai, K. I. Suga, and K. Kindo, Low-magnetoresistance RuO_2-Al_2O_3 thin-film thermometer and its application, Int. J. Thermophys. **30**, 316 (2009).

[49] J. Nelson and A. M. Goldman, Thin film cryogenic thermometers defined with optical lithography for thermomagnetic measurements on films, Rev. Sci. Instrum. **86**, 053902 (2015).

[50] S. Maniv and W. D. Westwood, Oxidation of an aluminum magnetron sputtering target in Ar/O_2 mixtures, J. Appl. Phys. **51**, 718 (1980).

[51] E. Wallin and U. Helmersson, Hysteresis-free reactive high power impulse magnetron sputtering, Thin Solid Films **516**, 6398 (2008).

[52] Except for this procedure, we do not need to be extremely careful about the maintenance of the RuO_2 and Al targets. As a side note, during the presputtering process, RuO_2 thin flakes that are easily peeled off may form on the shutter in the sputtering chamber, so we need to clean it regularly to prevent these flakes from falling on the RuO_2 target.

[53] M. Voigt and M. Sokolowski, Electrical properties of thin rf sputtered aluminum oxide films, Mater. Sci. Eng.: B **109**, 99 (2004).

[54] Since the SPE measurement in this study was intended to be performed at 2 K, the conditions for the thermometer fabrication were chosen to realize high sensitivity at 2 K. Our method can be extended to different temperatures by making thermometer films with high sensitivity at the targeted temperature range. However, as the temperature is lowered toward zero kelvin, the SPE-induced temperature difference is expected to decrease because the population of thermal magnons in YIG is suppressed.

[55] A. Hoffmann, Spin Hall effects in metals, IEEE Trans. Magn. **49**, 5172 (2013).

[56] J. Sinova, S. O. Valenzuela, J. Wunderlich, C. H. Back, and T. Jungwirth, Spin Hall effects, Rev. Mod. Phys. **87**, 1213 (2015).

[57] M. Schreier, G. E. W. Bauer, V. I. Vasyuchka, J. Flipse, K. Uchida, J. Lotze, V. Lauer, A. V. Chumak, A. A. Serga, S. Daimon, T. Kikkawa, E. Saitoh, B. J. van Wees, B. Hillebrands, R. Gross, and S. T. B. Goennenwein, Sign of inverse spin Hall voltages generated by ferromagnetic resonance and temperature gradients in yttrium iron garnet platinum bilayers, J. Phys. D: Appl. Phys. **48**, 025001 (2015).

[58] The Joule-heating-induced temperature increase under a typical ΔJ_c value of 0.15 mA is less than 10 mK, which was confirmed by measuring the R_{TM} value of the RuO_2-AlO_x film under the dc current of 0.15 mA applied to the Pt wire at $T = 2$ K and by comparing it with the R_{TM}-T calibration curve shown in Fig. 4(d). The current value of 0.15 mA was adopted such that the sample's temperature increase is less than 1% compared to the base temperature of 2 K and also that the SPE signal can be measured with a sufficient signal-to-noise ratio.

[59] For the delay time of $\tau_{\mathrm{delay}} = 50$ ms and the data acquisition time $\tau_{\mathrm{sens}} = 20$ ms, the frequency of the applied square-wave current is estimated to be $f = 1/2(\tau_{\mathrm{delay}} + \tau_{\mathrm{sens}}) \sim 7$ Hz.

[60] N. F. Mott, Conduction in non-crystalline materials III. Localized states in a pseudogap and near extremities of conduction and valence bands, Philos. Mag. **19**, 835 (1969).

[61] V. Ambegaokar, B. I. Halperin, and J. S. Langer, Hopping conductivity in disordered systems, Phys. Rev. B **4**, 2612 (1971).

[62] R. Rosenbaum, Crossover from Mott to Efros-Shklovskii variable-range-hopping conductivity in In_xO_y films, Phys. Rev. B **44**, 3599 (1991).

[63] S. Lafuerza, J. García, G. Subías, J. Blasco, K. Conder, and E. Pomjakushina, Intrinsic electrical properties of $LuFe_2O_4$, Phys. Rev. B **88**, 085130 (2013).

[64] C. Lu, A. Quindeau, H. Deniz, D. Preziosi, D. Hesse, and M. Alexe, Crossover of conduction mechanism in Sr_2IrO_4 epitaxial thin films, Appl. Phys. Lett. **105**, 082407 (2014).

[65] X. Chen, B. Wang, Y. Chen, H. Wei, and B. Cao, Tuning Jahn–Teller distortion and electron localization of $LaMnO_3$ epitaxial films via substrate temperature, J. Phys. D: Appl. Phys. **54**, 235302 (2021).

[66] Y. Li, M. You, X. Li, B. Yang, Z. Lin, and J. Liu, Tunable sensitivity of zirconium oxynitride thin-film temperature sensor modulated by film thickness, J. Mater. Sci.: Mater. Electron. **33**, 20940 (2022).

[67] C. T. Harris and T.-M. Lu, A PtNiGe resistance thermometer for cryogenic applications, Rev. Sci. Instrum. **92**, 054904 (2021).

[68] E. A. Scott, C. M. Smyth, M. K. Singh, T.-M. Lu, P. Sharma, D. Pete, J. Watt, and C. T. Harris, Optimization of gold germanium ($Au_{0.17}Ge_{0.83}$) thin films for high sensitivity resistance thermometry, J. Appl. Phys. **132**, 065103 (2022).

[69] S. S. Courts and P. R. Swinehart, Review of Cernox$^{\mathrm{TM}}$ (zirconium oxy-nitride) thin-film resistance temperature sensors, AIP Conf. Proc. **684**, 393 (2003).

[70] J. R. Clement and E. H. Quinnell, The low temperature characteristics of carbon-composition thermometers, Rev. Sci. Instrum. **23**, 213 (1952).

[71] W. N. Lawless, Thermometric properties of carbon-impregnated porous glass at low temperatures, Rev. Sci. Instrum. **43**, 1743 (1972).

[72] T. Kikkawa, M. Suzuki, J. Okabayashi, K. Uchida, D. Kikuchi, Z. Qiu, and E. Saitoh, Detection of induced paramagnetic moments in Pt on $Y_3Fe_5O_{12}$ via x-ray magnetic circular dichroism, Phys. Rev. B **95**, 214416 (2017).

[73] A typical error at each field is evaluated to be 9.8 mΩ for the data under $\Delta J_c = 0.15$ mA, so the slight undulation behavior of ΔR_{TM} above $B = 0.05$ T is attributed to the uncertainty of the measurement.

[74] K. Uchida, J. Ohe, T. Kikkawa, S. Daimon, D. Hou, Z. Qiu, and E. Saitoh, Intrinsic surface magnetic anisotropy in $Y_3Fe_5O_{12}$ as the origin of low-magnetic-field behavior of the spin Seebeck effect, Phys. Rev. B **92**, 014415 (2015).

[75] T. Kikkawa, K. Uchida, S. Daimon, Z. Qiu, Y. Shiomi, and E. Saitoh, Critical suppression of spin Seebeck effect by magnetic fields, Phys. Rev. B **92**, 064413 (2015).

[76] H. Jin, S. R. Boona, Z. Yang, R. C. Myers, and J. P. Heremans, Effect of the magnon dispersion on the longitudinal spin Seebeck effect in yttrium iron garnets, Phys. Rev. B **92**, 054436 (2015).

[77] T. Kikkawa, K. Uchida, S. Daimon, and E. Saitoh, Complete suppression of longitudinal spin Seebeck effect by frozen magnetization dynamics in $Y_3Fe_5O_{12}$, J. Phys. Soc. Jpn. **85**, 065003 (2016).

[78] H. Adachi, K. Uchida, E. Saitoh, and S. Maekawa, Theory of the spin Seebeck effect, Rep. Prog. Phys. **76**, 036501 (2013).

[79] S. A. Bender and Y. Tserkovnyak, Interfacial spin and heat transfer between metals and magnetic insulators, Phys. Rev. B **96**, 134412 (2015).

[80] L. J. Cornelissen, K. J. H. Peters, G. E. W. Bauer, R. A. Duine, and B. J. van Wees, Magnon spin transport driven by the magnon chemical potential in a magnetic insulator, Phys. Rev. B **94**, 014412 (2016).

[81] Y. Ohnuma, M. Matsuo, and S. Maekawa, Theory of the spin Peltier effect, Phys. Rev. B **96**, 134412 (2017).

[82] K. Kanahashi, J. Pu, and T. Takenobu, 2D materials for large-area flexible thermoelectric devices, Adv. Energy Mater. **10**, 1902842 (2020).

[83] D. Li, Y. Gong, Y. Chen, J. Lin, Q. Khan, Y. Zhang, Y. Li, H. Zhang, and H. Xie, Recent progress of two-dimensional thermoelectric materials, Nano-Micro Lett. **12**, 36 (2020).

[84] Q. H. Wang, A. Bedoya-Pinto, M. Blei, A. H. Dismukes, A. Hamo, S. Jenkins, M. Koperski, Y. Liu, Q.-C. Sun, and E. J. Telford, *et al.*, The magnetic genome of two-dimensional van der Waals materials, ACS Nano **16**, 6960 (2022).